Pergamon

Acta Materialia 50 (2002) 1581–1586

Acta MATERIALIA

www.actamat-journals.com

Small-angle neutron scattering of precipitates in Ni–Ti shape memory alloys

M. Kompatscher [a], B. Demé [b], G. Kostorz [a,*], Ch. Somsen [c], E.F. Wassermann [c]

[a] *ETH Zürich, Institut für Angewandte Physik, CH-8093 Zürich, Switzerland*
[b] *Institut Laue-Langevin, F-38042 Grenoble, France*
[c] *Gerhard-Mercator-Universität, Tieftemperaturphysik, D-47048 Duisburg, Germany*

Received 28 June 2001; received in revised form 10 December 2001; accepted 13 December 2001

Abstract

Small-angle neutron scattering was performed on polycrystals of Ni–(46–49) at.% Ti quenched in ice water from the solid solution. The presence of small precipitates of a radius of about 1 nm was found for Ni–(46, 47 and 48) at.% Ti. Assuming a composition of Ni_4Ti_3 of the precipitates, their volume fraction varies from 7% to 0.3%. No precipitates are found if the Ti content is closer to stoichiometric NiTi. The formation of these precipitates already during quenching seems to suppress the formation of martensite. Ni–(47.9 and 48.5) at.% Ti were further aged for 1 h at 553 K, and small-angle scattering shows a fully established precipitate microstructure. The particles have a radius of about 1.5 nm and a mean interparticle distance of 4.8–5.8 nm. From the integrated small-angle scattering curves, a volume fraction of Ni_4Ti_3 particles of about 20% is obtained. © 2002 Acta Materialia Inc. Published by Elsevier Science Ltd. All rights reserved.

Keywords: Alloys (nickel, titanium); Small-angle neutron scattering; Phase transformations

1. Introduction

The martensitic phase transitions (MTs) in B2-structured Ni–Ti shape memory alloys depend strongly on composition and heat treatment [1]. Fig. 1 shows the partial structural phase diagram of Ni–Ti [2]. The high-temperature NiTi phase has the ordered body centered cubic (B2) structure. In the two-phase regime below the stability range of the B2 structure, Ni-rich off-stoichiometric Ni–Ti follows the decomposition sequence: Ni–Ti→matrix+Ni_4Ti_3→matrix+Ni_3Ti_2→matrix+$\underline{N}i_3Ti$ (stable) [3]. Ni_4Ti_3 belongs to space group $R\bar{3}$ with a rhombohedral unit cell [4,5]. These precipitates are known to improve shape memory behavior, influencing the MT sequence and transformation temperatures [6,7].

For quenched samples (out of the NiTi phase stability range), an MT from the NiTi phase to the B19′ phase (monoclinic structure) occurs up to about Ni–49 at.% Ti. The martensitic start temperatures are plotted as triangles in Fig. 1 [8]. The quenched samples with lower Ti concentration

* Corresponding author. Tel. +41-1-633-3399; fax: +41-1-633-1105.
E-mail address: kostorz@iap.phys.ethz.ch (G. Kostorz).

1359-6454/02/$22.00 © 2002 Acta Materialia Inc. Published by Elsevier Science Ltd. All rights reserved.
PII: S1359-6454(02)00019-8

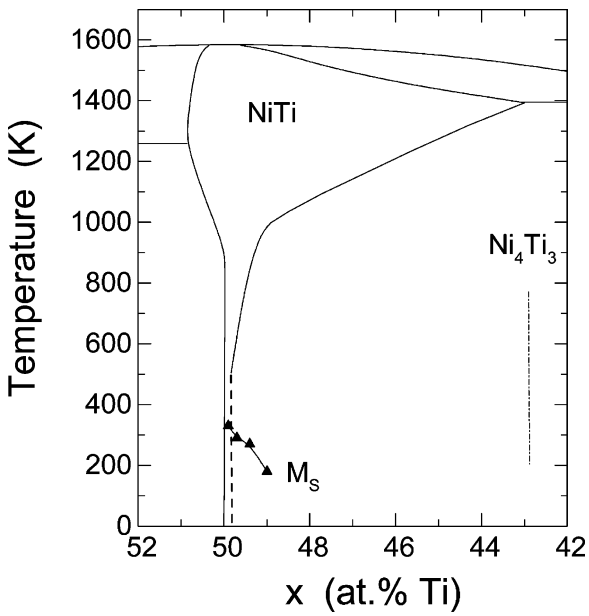

Fig. 1. Partial structural phase diagram of Ni–Ti [2]. (———) taken from [14], (- - -) from [15] indicate a stability of the B2 phase down to low temperatures. The composition of the metastable Ni_4Ti_3 [3] is marked by a vertical – · – line. The MT start temperatures M_s for quenched samples after [8] are indicated with ▲.

show an anomaly in the electrical resistivity as a function of temperature [2]. The resistivity increases from ambient temperature down to 4 K by about 40%, without any noticeable hysteresis upon warm-up, so there are no traces of martensite. However, electron diffraction patterns of quenched Ni–48 at.% Ti show two types of reflections beside the expected reflections of the B2 structure [9]. One type of reflections can be attributed to static lattice displacement waves which are precursors of the martensitic B19′ phase and the R phase, respectively. The other type of reflections, more diffuse in intensity, are located near 1/7<321> positions in reciprocal space indicating that small Ni_4Ti_3 precipitates are present inside the quenched specimen. This observation prompted a thorough search for small precipitates/clusters a few nm in size in these alloys.

Small-angle neutron scattering (SANS, see, e.g. [10]) is especially suited to study early stages of precipitation in Ni–Ti as Ni and Ti have scattering lengths of opposite signs. The scattering contrast is thus unusually large and correspondingly small volume fractions of a second phase may be identified. In the present study, the microstructure in the 'as quenched' state of five alloys, samples Q1–Q5, with different Ti content was investigated by SANS. Two annealed samples (1 h at 553 K after previous quenching in water from 1273 K, called A1 and A2) were also studied to provide a reference for a well-established microstructure, with Ni_4Ti_3 precipitates as revealed by transmission electron microscopy [11].

2. Experimental procedure

Ni–Ti polycrystals with nominal concentrations between 46 and 49 at.% Ti were prepared by arc melting in an Ar atmosphere. The samples (disks 7–9 mm in diameter, 3 mm thick) were encapsulated in quartz tubes (500 mbar Ar), solution treated at 1273 K for 1 h and then quenched in ice water. Two samples (A1, A2) were further annealed for 1 h at 553 K and then again quenched. All samples were finally mechanically polished with 3 μm diamond paste and checked for their concentration by calibrated X-ray fluorescence analysis (Table 1).

All samples were studied on the small-angle scattering instrument D22 of the ILL, Grenoble. The samples were placed on a sample changer in a vacuum chamber and measured at room temperature. Thus, background scattering was as low as possible. The diameter of the incident beam was reduced to 9 mm by a Cd aperture and in front of each sample, a further Cd aperture, 6 mm in diameter, was mounted to define the illuminated area. An incident wavelength $\lambda = 0.8$ nm (spread in wavelength of 10% full width at half maximum) was used to avoid double-Bragg scattering from the B2 structure of the matrix. The modulus of the scattering vector, $Q = 4\pi\sin\theta/\lambda$ (where θ is half the scattering angle), covered a range of $0.1 < Q/\mathrm{nm}^{-1} < 3$, after combination of results from two different sample-to-detector distances (1.42 and 5.67 m). All scattering patterns were taken with a two-dimensional position-sensitive He^3 detector, corrected for background scattering and electronic noise, and converted to absolute macro-

Table 1
Mean particle radius as evaluated by the Guinier analysis of the measured scattering curves of as-quenched samples Q1–Q5, and calculated volume fractions and particle densities of assumed Ni_4Ti_3 precipitates. Average sample compositions are measured by calibrated X-ray fluorescence analysis. Mean particle size and distance of the precipitates as evaluated from the correlation function of aged samples A1 and A2, and corresponding volume fractions and particle densities as calculated from the integrated intensity

Sample	Ti content (at.%)	Particle radius (nm)	Particle distance (nm)	Volume fraction (%)	Particle density (10^{-3} nm^{-3})
Q1	49.0 (1)	–	–	–	–
Q2	48.4 (1)	0.9 (4)	–	0.3 (3)	1 (1)
Q3	47.9 (1)	1.1 (1)	–	0.6 (2)	1.1 (5)
Q4	47.0 (1)	1.2 (1)	–	3 (1)	4 (2)
Q5	46.0 (1)	1.3 (1)	–	7 (2)	8 (3)
A1	48.5 (1)	1.55 (1)	5.78 (5)	17.2 (5)	11.0 (4)
A2	47.9 (1)	1.38 (2)	4.83 (5)	21.6 (5)	19.6 (9)

scopic differential scattering cross sections after calibration with the incoherent scattering of a vanadium single crystal.

3. Results and discussion

The total sample-related scattering $I(Q)$ is composed of an incoherent scattering contribution I_{inc} of all elements in the sample, a Laue scattering term I_L, and the term of interest in SANS, given as the coherent elastic macroscopic differential SANS cross section I_{coh}.

The Laue scattering contribution I_L for the Ni-rich Ni–Ti alloys is calculated, assuming a Ni sublattice fully occupied by Ni atoms and a Ti sublattice where the excess Ni atoms are accommodated as antisite defects, i.e. $Ni(Ti_{1-2x}Ni_{2x})$ with x the Ni content in excess of the stoichiometric composition. First-principles calculations on a similar alloy [12] suggest the absence of structural vacancies on the Ni-rich side of the phase diagram, thus

$$I_L = \frac{1}{a^3}[2x(1-2x)(\Delta b)^2] \quad (1)$$

where a is the lattice parameter of the B2 phase and Δb the bound coherent scattering length difference of the two components.

Experimentally, the constant 'background' $I_B = I_{inc} + I_L$ was determined from Porod plots, i.e., from plotting the scattering curves $I(Q)$ obtained by averaging over rings of equal Q in the form of $I(Q)\ Q^4$ versus Q^4 (Fig. 2). In the Q range where the intensity can be expressed as $I(Q) = A/Q^4 + I_B$ (Porod's law) these plots will be linear; their slopes contain the Q-independent I_B. Values of I_B determined from these plots are within 10% of the calculated values based on tabulated cross-sections.

The finally resulting cross-sections I_{coh} for all samples are shown in Fig. 3. A Q^{-4}-dependence of the scattering intensity is observed for scattering vectors smaller than 0.5 nm^{-1}. Such scattering is frequently observed for polycrystals and usually related to a few large precipitates at grain bound-

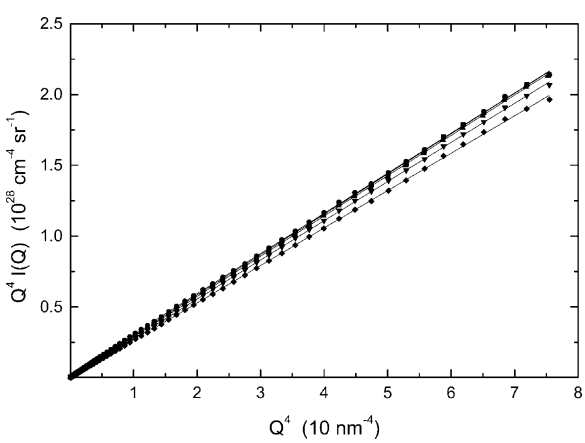

Fig. 2. Porod plots of 'as-quenched' samples Q1–Q5 (heat treated for 1 h at 1273 K). (◆) Ni–49 at.% Ti, (▼) Ni–48.4 at.% Ti, (▲) Ni–47.9 at.% Ti, (■) Ni–47 at.% Ti, (●) Ni–46 at.% Ti.

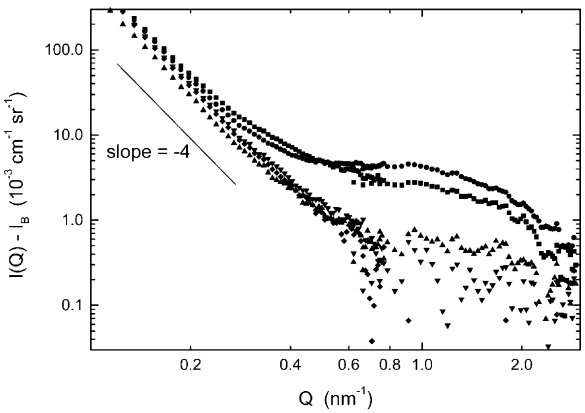

Fig. 3. Macroscopic coherent elastic differential SANS cross sections $I_{coh} = I(Q) - I_B$ of 'as-quenched' samples Q1–Q5 (heat treated for 1 h at 1273 K). (◆) Ni–49 at.% Ti, (▼) Ni–48.4 at.% Ti, (▲) Ni–47.9 at.% Ti, (■) Ni–47 at.% Ti, (●) Ni–46 at.% Ti.

aries, dislocations and other inhomogeneities. For the sample Q1, no significant additional scattering contribution is observed. For the other solution treated samples (Q2–Q5), a small increase of coherent scattering is observable and a Guinier analysis (see, e.g. [10]) is applicable (Fig. 4). For a two-phase mixture with monodisperse particles, I_{coh} is expressed as

$$I_{coh} = C_p V_p (\rho_{bp} - \rho_{bm})^2 \exp(-Q^2 R_g^2/3) \quad (2)$$

where C_p is the volume fraction of the precipitates

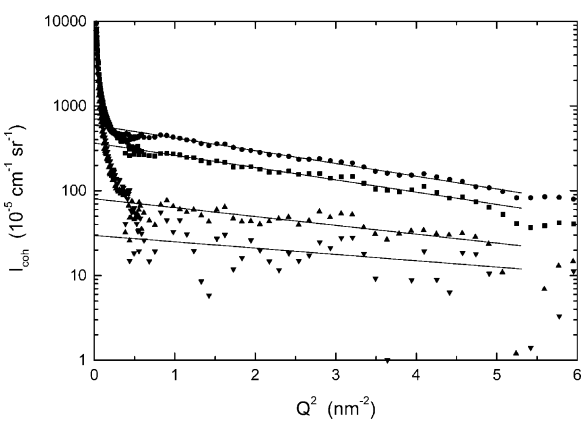

Fig. 4. Guinier plots of the 'as-quenched' samples Q2–Q5 (heat treated for 1 h at 1273 K). Straight lines are fits of the scattering function (2) to the data. (▼) Ni–48.4 at.% Ti, (▲) Ni–47.9 at.% Ti, (■) Ni–47 at.% Ti, (●) Ni–46 at.% Ti.

in the sample, $(\rho_{bp} - \rho_{bm})$ the difference between the homogeneous scattering length densities of the particles and of the matrix, V_p the volume of a single precipitate, and R_g the radius of gyration. For spherical particles, R_g is related to the average radius of a sphere, R_s, by $R_g^2 = 3R_s^2/5$.

The volume fraction of the precipitates is obtained by extrapolation of the scattering function (2) to the origin of reciprocal space. Assuming a composition of Ni_4Ti_3 for the particles and the nominal composition for the matrix (as C_p is very small),

$$C_p = \frac{I_{coh}(0)}{V_p(\rho_{bp} - \rho_{bm})^2}. \quad (3)$$

The radii for spherical precipitates, their volume fractions and their densities n $(=C_p/V_p)$ are listed for samples Q2–Q5 in Table 1. For samples Q4 and Q5 with the highest compositional deviation from stoichiometry, a considerable volume fraction is obtained, and some correlations between the precipitates are reflected in the scattering curve (see the weak broad peaks in Fig. 4). This adds an uncertainty to the slope of the Guinier plot. The upper and lower limits given in Table 1 include these possible errors.

Fig. 5 shows the volume of a single precipitate V_p and the volume fraction C_p of these precipitates as a function of the average Ti concentration of the samples. Both V_p and C_p start to increase from about 49 at.% Ti with decreasing Ti concentration.

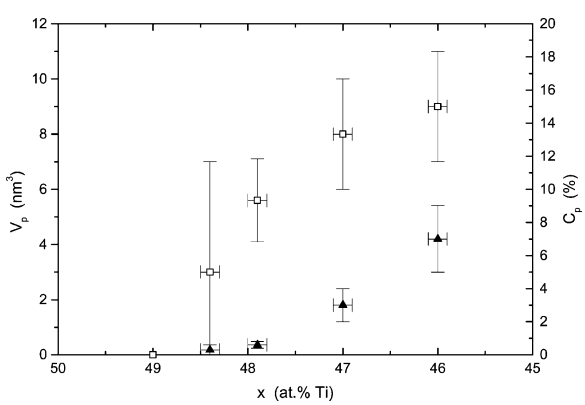

Fig. 5. (□) Volume V_p of a single precipitate and (▲) volume fraction C_p as a function of the average Ti-concentration of NiTi alloys after quenching from 1273 K in ice water.

It is important to note that the MT to the B19′ phase abruptly vanishes at about 49 at.% Ti for all lower Ti concentrations, associated with the detection of the Ni_4Ti_3 precipitates. From this it is inferred that these precipitates in an early stage of formation suppress the MT for quenched Ni-rich alloys.

For the aged samples A1 and A2 a peak at $Q \neq 0$ occurs in the scattering curves (Fig. 6). Such peaks indicate strong particle–particle correlations in the decomposed samples. A Guinier evaluation is not applicable because of the unknown interparticle interference function. Fitting the measured scattering curves by a small number of Hermitian functions [13] provides for an easy Fourier transformation of the scattering function to get the correlation function. In Fig. 7 the correlation functions for A1 and A2 are shown. The position of the first minimum can be taken as a measure for the typical particle size and the position of the first maximum reflects the most probable interparticle distance (see Table 1).

For the aged samples, the data are sufficiently precise to determine the integrated intensity. Integrating the scattering curves over all scattering vectors, using Porod's law for large scattering vectors, gives the integrated intensity $\tilde{Q}$, representing the mean-square fluctuation of the scattering length density of the system and given for the two-phase case by

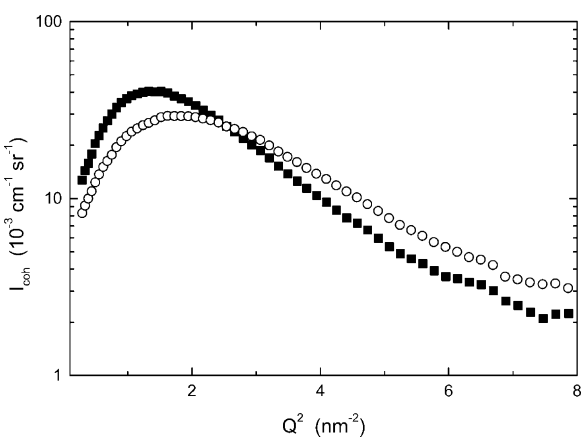

Fig. 6. Guinier plots of samples A1 and A2 (aged for 1 h at 553 K, after a previous quench in water from 1273 K). (■) Ni–48.5 at.% Ti (A1), (○) Ni–47.9 at.% Ti (A2).

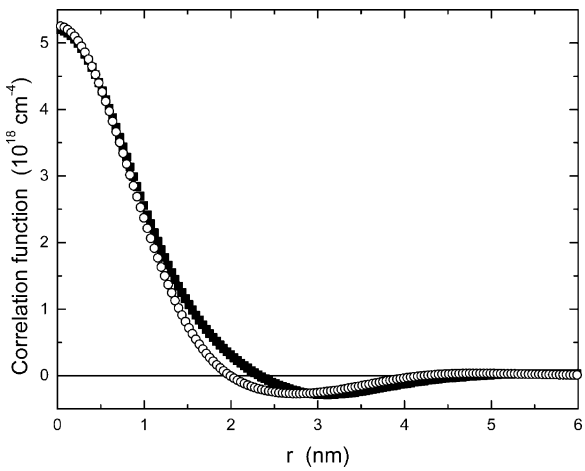

Fig. 7. Correlation functions of samples A1 and A2 (aged for 1 h at 553 K, after a previous quench in water from 1273 K) after Fourier transformation of the scattering function, fitted by a small number of Hermitian functions [13]. (■) Ni–48.5 at.% Ti (A1), (○) Ni–47.9 at.% Ti (A2).

$$\tilde{Q} = (2\pi)^3\overline{|\Delta\rho|^2} = (2\pi)^3(c_p - \bar{c})(\bar{c} - c_m)|\rho_{Ni} - \rho_{Ti}|^2 \quad (4)$$

where $\Delta\rho$ is the scattering contrast between particle and matrix, $(\rho_{Ni}-\rho_{Ti})$ the difference of the atomic scattering length densities, c_p, c_m and $\bar{c}$ the Ti-concentration in the precipitates, in the matrix and of the total sample, respectively. Assuming again precipitates of Ni_4Ti_3, and knowing the average sample composition, the concentration of the matrix is obtained and thus the volume fraction of the precipitates applying the lever rule (see Table 1).

4. Conclusion

Ni–(46, 47 and 48) at.% Ti alloys quenched from 1273 K in ice water contain small precipitates of a radius of about 1 nm. If a composition of Ni_4Ti_3 is assumed, volume fractions vary from 7% (Ni–46 at.% Ti) to 0.3% (Ni–48.4 at.% Ti). No precipitates are found by SANS for quenched samples with Ti contents closer to stoichiometric NiTi. The occurrence of precipitates in an early stage of formation in quenched Ni-rich Ni–Ti alloys seems to suppress the formation of martensite.

Ni–(47.9 and 48.5) at.% Ti alloys aged for 1 h at 553 K after previous quenching from 1273 K, contain precipitates of a radius of about 1.5 nm with interparticle distances of 4.8–5.8 nm. If a particle composition of Ni_4Ti_3 is assumed, the volume fractions are 21.5% and 17% for the two alloys, respectively.

Acknowledgements

The authors are grateful to T. Kakeshita for providing the samples and to R. May and J.-M. Schneider for their important help in preparing the experiment. ILL Grenoble kindly provided beam time on the small-angle scattering instrument D22.

References

[1] Otsuka K, Ren X. Mater. Sci. Eng. A 1999;273–275:89.
[2] Somsen Ch, Zähres H, Kästner J, Wassermann EF, Kakeshita T, Saburi T. Mater. Sci. Eng. A 1999;273–275:310.
[3] Nishida M, Wayman CM, Honma T. Met. Trans. A 1986;17:1505.
[4] Tadaki T, Nakata Y, Shimizu K, Otsuka K. Trans. JIM 1986;27:731.
[5] Saburi T, Nenno S, Fukuda T. Less Com. Met. 1986;125:157.
[6] Miyazaki S, Ohmi Y, Otsuka K, Suzuki Y. J. Phys. 1982;43(C4):255.
[7] Saburi T, Tatsumi T, Nenno S. J. Phys. 1982;43(C4):261.
[8] Nishida M, Honma T. Scripta Metall. 1984;18:1293.
[9] Somsen C, Kästner J, Wassermann EF, Boullay P, Schryvers D. Proceedings of ESOMAT 2000, Como/Italy, in press.
[10] Kostorz G. X-ray and neutron scattering. In: Chan RW, Haasen P, editors. Physical metallurgy. 4th ed. Amsterdam: North-Holland; 1996. p. 1115.
[11] Zel'dovich V, Sobyanina G, Novoselova TV. J. Phys. IV 1997;C5:299.
[12] Meyer B, Fähnle M. Phys. Rev. B 1999;59(9):6072.
[13] Svergun DI. J. Appl. Cryst. 1993;26:258.
[14] Murray JL. In: Nash P, editor. Phase diagrams of binary nickel alloys. Materials Park, OH: ASM; 1991. p. 342.
[15] Treppmann D. Thermomechanical treatment of NiTi, in VDI-Fortschrittberichte, Reihe 5, Nr. 462, VDI-Verlag, 1997:147.